Journal Pre-proof

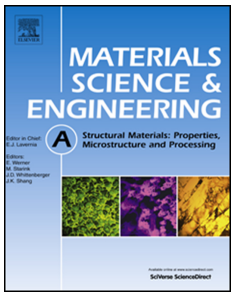

Out-of-Phase Thermomechanical Fatigue of a Single Crystal Ni-Base Superalloy

M. Sirrenberg, D. Bürger, S. Guth, T. Babinský, P. Thome, A.B. Parsa, G. Eggeler

PII: S0921-5093(24)00782-2

DOI: https://doi.org/10.1016/j.msea.2024.146851

Reference: MSA 146851

To appear in: *Materials Science & Engineering A*

Received Date: 1 February 2024

Revised Date: 19 May 2024

Accepted Date: 17 June 2024

Please cite this article as: M. Sirrenberg, D. Bürger, S. Guth, T. Babinský, P. Thome, A.B. Parsa, G. Eggeler, Out-of-Phase Thermomechanical Fatigue of a Single Crystal Ni-Base Superalloy, *Materials Science & Engineering A*, https://doi.org/10.1016/j.msea.2024.146851.

Out-of-Phase Thermomechanical Fatigue of a Single Crystal Ni-Base Superalloy

M. Sirrenberg[1*], D. Bürger[1], S. Guth[2], T. Babinský[3], P. Thome[1], A.B. Parsa[1], G. Eggeler[1]

1 Institut für Werkstoffe, Ruhr-Universität Bochum, Universitätsstr. 150, 44801 Bochum, Germany

2 Institut für Angewandte Materialien – Werkstoffkunde, Karlsruher Institut für Technologie, Engelbert-Arnold-Straße 4, 76131 Karlsruhe, Germany

3 Institute of Physics of Materials, Czech Academy of Sciences, Žižkova 513/22, 61600 Brno, Czech Republic

* Corresponding author: marc.sirrenberg@rub.de

Abstract

The present work studies the out-of-phase thermomechanical fatigue (OP-TMF) behavior of the precisely oriented [001] single crystal Ni-base superalloy ERBO/1 (CMSX-4 type). The OP-TMF tests are performed between minimum and maximum temperatures of 1023 and 1223 K and a cyclic mechanical strain amplitude of ±0.5%. In accordance with previous findings, the present study confirmed that isothermal low cycle fatigue (LCF) tests at 1023 and 1223 K show significantly longer fatigue lives than the OP-TMF tests, specimens with rougher surfaces fail earlier than polished specimens and deformation bands and cracks form in the specimen surface. Two new results were obtained: First, when comparing OP-TMF cycles with fast cooling (tensile part of cycle) and fast vs. slow heating (compressive part of cycle) one finds that the slower heating/compressive cycle is more damaging. Second, analytical scanning electron microscopy of the flanks of an OP-TMF crack allows to study the diffusion-controlled growth kinetics of the oxide and the underlying zone, which is depleted by the oxide forming elements. These results are discussed in the light of the microstructural, mechanical and chemical results of the present study considering previous work on OP-TMF of superalloy single crystals (SXs).

Key Words: Superalloy single crystals, Out-of-phase thermomechanical fatigue, Surface roughness, Cycle shapes, Oxidation.

1. Introduction

Ni-base single crystal superalloys (SXs) are used to make blades for gas turbines operating in aero engines and powerplants [e.g. 1-7]. They are mechanically loaded at high temperatures not too far from their melting point. The lifetime of SX components is often determined by start-up and shut-down events, which lead to thermomechanical fatigue (TMF). During engine start-up, temperatures increase in the surface of critical components like blades. These surface regions are constrained by the inner parts of the component, which are colder. The resulting mismatch of thermal strains causes transient compressive stresses. Similarly, an engine shut-down causes the temperatures in surface regions to decrease, while the inner bulk regions are still hot. Therefore, during cooling, increasing tensile stresses arise at the surface. In laboratory experiments this type of loading is best simulated by out-of-phase TMF experiments (OP-TMF), where temperature increases as strain simultaneously decreases and vice versa. In in-phase TMF experiments (IP-TMF), temperature and strain increase and decrease simultaneously. IP-TMF arises also due to varying temperatures in hot going components and represents the loading situation at internally cooled surfaces, e.g. at the inner surface of internally cooled turbine blades. High temperature fatigue has been identified as an important life-limiting factor for high temperature components [8-39] and especially non-isothermal fatigue tests have received attention. Both, out-of-phase and in-phase cycling have been studied, and both were shown to shorten fatigue life as compared to isothermal LCF conditions. For Ni-base SXs, it is often reported that for a given temperature range OP-TMF is the most damaging TMF load case [23,24,39]. For a temperature cycle with a relatively low maximum temperature of 1173 K, Okazaki et al. [28] found slightly shorter IP-lifetimes than OP-lifetimes. However, since OP-TMF represents the situation at the outer surface, which is subjected to higher maximum temperatures than the cooled inner surface represented by IP-TMF, OP-TMF is typically the life-limiting factor for turbine blades made of Ni-base SXs. Therefore, this study focusses on OP-TMF. In order to mimic steady state operation between start-up and shut-down, hold times at maximum temperature can be introduced. Under OP-TMF conditions, the hold times occur in the compressive regime and typically shorten cyclic fatigue life [29,40-43]. It has been reported and discussed in the literature, that high temperature oxidation is of central importance in both fatigue crack initiation and growth [15,19,21,27,32,39]. It has also been reported that under OP-TMF conditions cracks propagate along microtwins [29,30,33,44], which form due to a coupled dislocation glide and diffusion process [44-46]. Most of OP-TMF life is spent in the crack propagation stage [21,26,33] and the maximum tensile stresses at the lowest OP-TMF temperature are of utmost importance [31,32]. Usually, strain-controlled TMF tests employ triangle-shaped cycles for temperatures and mechanical loads. However, the actual loading conditions of a high temperature component may better be represented by other cycle shapes. Thus, heating and cooling rates can vary. In isothermal fatigue tests of a polycrystalline Ni-base superalloy, a strong influence of the cycle shape was found [38]. In the present work we subject the SX ERBO/1 (CMSX-4 type) [47] to isothermal and OP-TMF loading. To minimize scatter associated with specimen orientations, we work with precisely [001]-oriented specimens and consider the effect of surface quality. Instead of considering the effect of compression hold periods on cyclic life, we

compare the behavior of strain-controlled OP-TMF experiments with different heating rates in the compressive part of the cycle. We consider the evolution of stress-strain hysteresis loops and perform microstructural investigations in the scanning electron microscope (SEM) addressing the formation of cracks during fatigue loading. The results are discussed in the light of the mechanical and microstructural results obtained in the present work and in the light of previous work published in the literature.

2. Material and Experiments

2.1 Alloy, heat treatment and scanning electron microscopy

The material investigated in the present work was an alloy of CMSX-4 type, referred to as ERBO/1 [47]. The alloy was carefully chemically and microstructurally analyzed [47].

Its nominal chemical composition is given in Table 1. The material was received from Doncasters Bochum as single crystalline as-cast rods of 160 mm lengths and diameters of 20 mm.

Table 1: Chemical composition of alloy ERBO/1.

Element / wt.-%	Al	Co	Cr	Hf	Mo	Re	Ta	Ti	W	Ni
As-specified	5.45 - 5.75	9.3 - 10.0	6.4 - 6.6	0.07 - 0.12	0.5 - 0.7	2.8 - 3.1	6.3 - 6.7	0.9 - 1.1	6.2 - 6.6	Bal.

The rods were subjected to a solution heat treatment consisting of two hours annealing at 1573 K, slow heating (1 K/min) to 1583 K, six hours annealing at 1583 K followed by air cooling. The solution annealing was followed by a dual step precipitation heat treatment with four hours at 1413 K and 16 hours at 1143 K. The first step establishes volume fractions, γ'-particle sizes and γ-channel widths. The second step establishes chemical equilibria between the γ- and γ'-phase regions.

Microstructural investigations were performed using a SEM of type Leo Gemini 1530 VP from Carl Zeiss AG. This SEM is equipped with a field emission gun (FEG) and an in-lens detector. The SEM was used to characterize the γ/γ'-microstructure of the material prior to testing (on polished (001)-cross sections, perpendicular to the loading direction), to study the size distribution of small surface cracks (on the surface of OP-TMF specimens) and to study the formation of macro cracks during TMF loading (on (100)-cross sections, parallel to the loading direction). Good secondary electron contrast between the γ- and the γ'-phase was obtained by etching the metallographic cross sections for 3 s in a solution of 40 ml H_2O, 20 ml HCl (37%) and 10 ml H_2O_2. The γ/γ'-microstructure in a dendritic region of the material investigated in the present work prior to fatigue testing is shown in Figure 1. Figure 1a shows a SEM micrograph, where dark cuboidal γ'-particles are separated by brighter γ-channels.

Quantitative metallography was used to measure the size distributions of γ'-particles and γ-channel widths, an example for the distribution of γ'-particle sizes is shown in Figure 1b. From this type of quantitative measurements γ' and γ phase volume fractions were determined as 66 and 34%, respectively. Scanning electron microscopy was also used to study fatigue cracks on surfaces of TMF specimens and from (100)-cross sections. The distribution of lengths of small surface cracks was also evaluated quantitatively, measuring the lengths of several hundred micro cracks on micrographs of OP-TMF specimen surfaces. Particle size distributions and surface crack length distributions were evaluated using the image analysis software Imagic IMS [48].

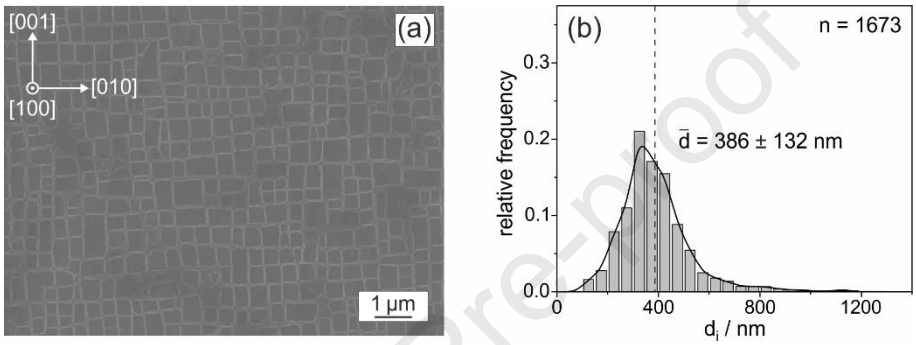

Figure 1: γ/γ'-microstructure prior to fatigue testing. (a) Secondary electron contrast SEM micrograph of the γ/γ'-microstructure (dendritic region) prior to fatigue testing. (b) γ'-particle size distribution of the investigated material. The mean particle size $\bar{d}$ is indicated by a dashed line.

Furthermore, high resolution orientation imaging microscopy using the rotation vector base line electron back scatter diffraction (RVB-EBSD) method [49], which allows to differentiate between crystal orientations as small as 0.03°, was performed using a SEM of QUANTA 650 from FEI, equipped with a field emission gun. All details describing our EBSD procedure have been described elsewhere [49-51].

During directional solidification of Ni-base superalloys, <001> represents a natural solidification direction, from which deviations of up to 10° can occur [5]. These small deviations affect the response to mechanical loading, as has been recently demonstrated for creep conditions by Heep et al. [52]. Therefore, we use an iterative procedure, where we orient the as-cast and heat treated material with the help of a Laue camera and then use electro discharge machining to machine precisely oriented [001] rods with diameters of 11 mm (maximum deviation from the targeted [001] direction: 2°), following the procedure described by Wollgramm et al. [53,54]. After the multiple step heat treatment, the pronounced chemical heterogeneity between prior dendritic and interdendritic regions, which characterizes the as-cast material state, is significantly reduced. For the material used in the present work this has been demonstrated using micro probe analysis [47,55]. The remaining differences in local alloy chemistry between dendritic and interdendritic regions occur on a length scale of the order of 100 µm, which is significantly smaller than the specimen

dimensions used for OP-TMF testing. This allows to exclude OP-TMF data scatter associated with chemical differences between different OP-TMF specimens.

2.2 Isothermal and Thermomechanical Fatigue Testing

From the as-cast, heat treated and oriented 11 mm diameter rods, cylindrical OP-TMF specimens were machined as shown in Figure 2a (gauge length: 15 mm, diameter: 5 mm).

Fatigue specimens were machined using a turning lathe. A photograph of a fatigue specimen is shown in Figure 2a. Figure 2b shows a fatigue specimen as mounted in the test rig used in the present work.

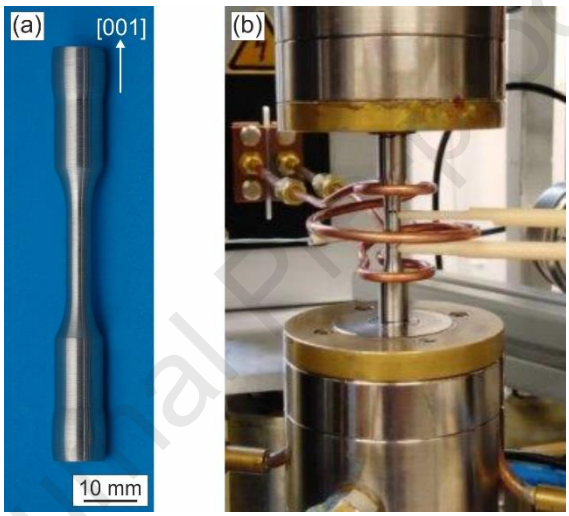

Figure 2: Photographs illustrating the fatigue testing setup. (a) Precisely oriented fatigue specimen (longitudinal direction: [001]). (b) Specimen as mounted into the fatigue test rig prior to testing.

Four fatigue specimens were tested in the as-machined condition. The surfaces of another set of six specimens were initially ground with emery paper up to a grit size of 600, then polished with diamond paste up to a grain size of 3 µm and finally polished using an oxide polishing suspension. These two types of specimen surface qualities were investigated to assess the effect of surface roughness on fatigue. In the present work we refer to the two types of surface qualities as rough (RS) and polished surfaces (PS). The surfaces were characterized measuring surface roughness profiles with a laser scanning confocal microscope of type µsurf from NanoFocus. Figure 3 shows the depth profiles associated with the two types of surface treatments.

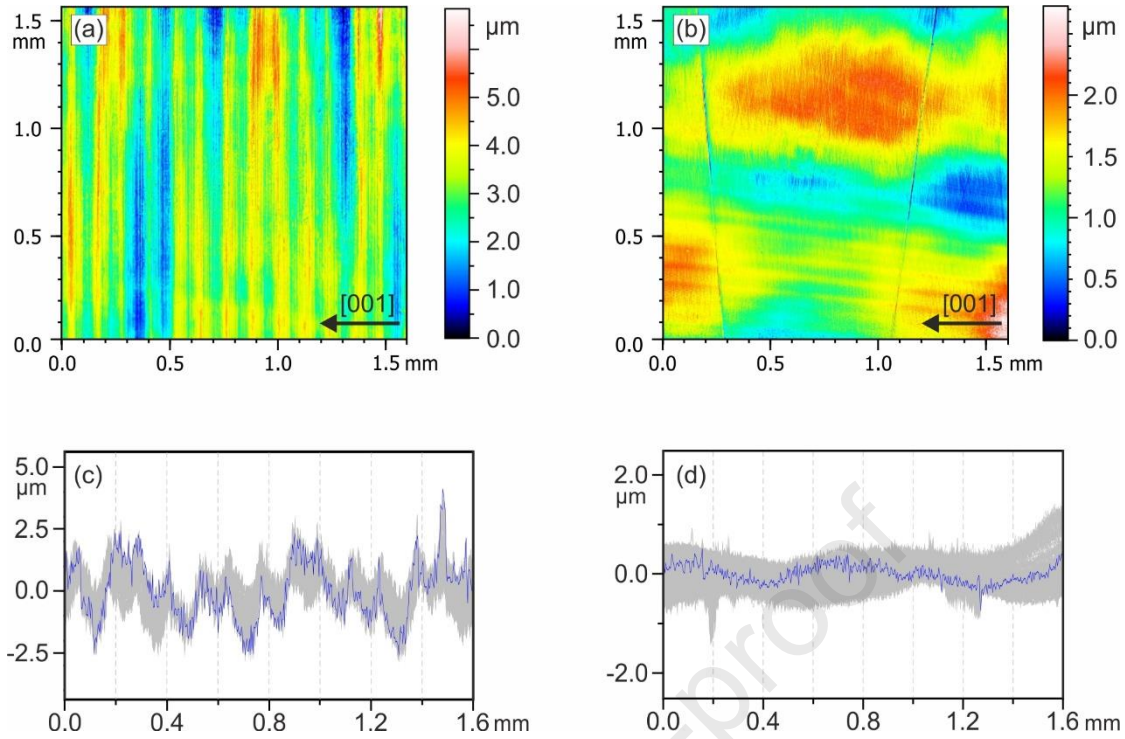

Figure 3: Depth profiles of the specimens with rough and polished surfaces. (a) and (b) Color coded depths results over 1.5 x 1.5 mm^2 areas. (c) and (d) Line profile of height values along a 1.5 mm reference line. (a) and (c) As-machined (rough) surface. (b) and (d) Polished surface.

From the surface profiles, the roughness parameters Ra (mean value of height deviations from average height) and Rz (maximum peak to valley difference in the profile) were determined [56]. The rougher surface was characterized by Ra/Rz-values of 0.43 and 3.43, respectively. For the polished surface these values were obtained as Ra=0.06 and Rz=0.65. Isothermal fatigue tests and out-of-phase TMF tests were performed under total mechanical strain control as described by Guth et al. [31-33], following the European code of practice [57], using a servo-electric test rig of type Zwick 1478. Figure 2b shows the induction coil which was used for heating to temperatures between 1023 to 1223 K (maximum heating power: 5 kW). The test temperature was measured and controlled with a NiCr/Ni thermocouple in direct contact with the specimen in the middle of the gauge length (contacting the specimen from behind in Figure 2b). As can be seen in Figure 2b, two sharp alumina rods transferred displacements to a water-cooled capacitive extensometer in a safe distance from the hot region. The alumina rods were slightly pushed against the specimen, in a tip-to-tip distance of 10 mm (gauge length), which did not cause any significant bending. The extensometer was used to measure and control the imposed strain. A mechanical strain amplitude of 0.5% was imposed in all tests, which runs from -0.5% in compression to +0.5% in tension (R_ε = -1). Isothermal tension/compression fatigue tests were performed at 1023 and 1223 K, at an imposed total strain rate of $3.33 \cdot 10^{-4}$ s^{-1} (duration of tensile and compressive parts of cycle: 30 and 60 s, respectively). In out-of-phase TMF testing, an effort was made to determine the thermal strain associated with thermal cycling under load-free conditions and controlling the experiment with only the mechanical strain [31]. Two types of heating/cooling cycles were compared. In

both types of experiments, the tensile/cooling part of the cycle had a duration of 30 s (cooling rate for all tests: 6.66 K/s, total strain rate: $3.33 \cdot 10^{-4}$ s^{-1}). The two tests differed in the imposed heating rates in the compressive parts of the cycles, which were fast (duration of heating period: 60 s, heating rate: 3.33 K/s, strain rate: $1.66 \cdot 10^{-4}$ s^{-1}) and slow (duration of heating period: 300 s, heating rate: 0.66 K/s, strain rate: $3.33 \cdot 10^{-5}$ s^{-1}). The strain and temperature profiles used for out-of-phase TMF testing are shown in Figures 4a and b. As indicated in Figures 4a and b we refer to the cycle type with the faster compressive part (duration: 60 s) as cycle type 1 and to the cycle type with the slower compressive part (duration: 300 s) as cycle type 2. No measures needed to be taken to enforce cooling in TMF testing from 1223 K to 1023 K in 30 s, because cooling by the ambient air and by the contact with the water-cooled grips was sufficient.

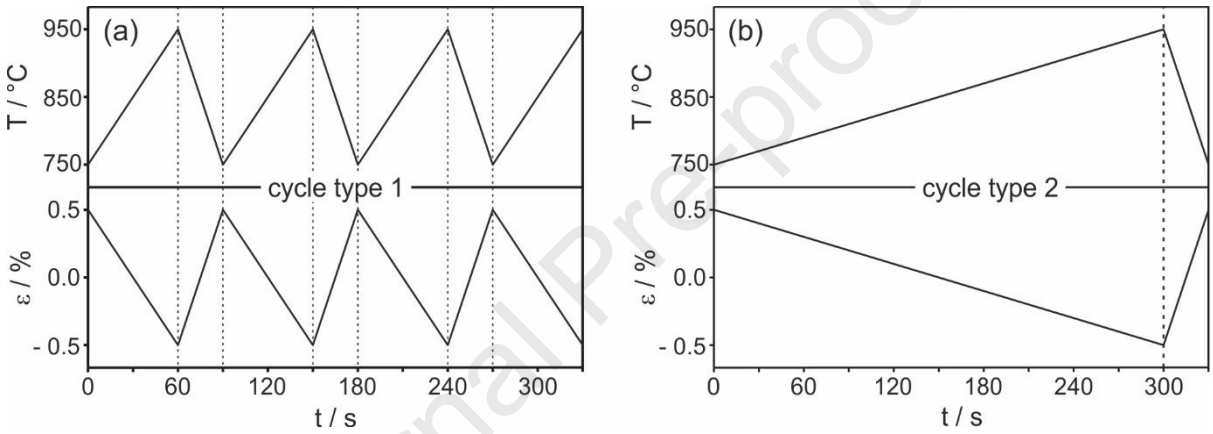

Figure 4: Two out-of-phase TMF conditions considered in the present work. Constant cooling rates were applied in the tensile parts of both types of TMF loading (duration: 30s). The two TMF conditions differed in the rate of heating in the compressive parts of the cycles. (a) Cycle type 1: TMF cycle with fast (60 s) heating in the compressive cycle. (b) Cycle type 2: TMF cycle with slow (300 s) heating in the compressive part of the cycle.

Table 2 lists the ten fatigue experiments, which were performed in the present work together with the failure lives. Note that the imposed ε(t)-profiles of the isothermal tests 1 and 2 are the same as those used for the TMF tests performed with cycle type 1 (fast heating in compressive part of cycle). The number of cycles to failure N_f, was evaluated for all tests using a 10% drop of the stabilized maximum stress as failure criterion. In some cases, the specimens fractured completely before a 10% drop of the maximum stress was reached. In that case the cycles to fracture were used as N_f.

Table 2: Ten fatigue tests, which were performed in the present work. Cycle type 1: Tensile part – 30 s, compressive part – 60 s, Cycle type 2: Tensile part – 30 s, compressive part – 300 s - Surface qualities: RS – as-machined rough surface, PS – polished smooth surface, imposed cycles: N – accumulated cycle number without failure, N_f – number of cycles to failure.

No	Type	Temperature/K	Cycle type	Surface quality	Imposed cycles
1	Isothermal	1023	1*	RS	N = 20000
2	"	1223	1*	"	N_f = 4072
3	TMF	1023 - 1223	1	"	N = 100
4	"	"	1	"	N = 1000
5	"	"	1	"	N_f = 2157
6	"	"	2	"	N_f = 996
7	"	"	1	PS	N = 1000
8	"	"	1	"	N_f = 5350
9	"	"	2	"	N = 1000
10	"	"	2	"	N_f = 3365

* Same imposed strain/time profile as in TMF cycle of type 1 (Figure 4a)

3. Results

3.1 Stress-strain hysteresis loops and fatigue life

Figure 5 shows stress-strain hysteresis loops which were measured after 500 cycles for specimens 5 (cycle type 1, fast heating) and 6 (cycle type 2, slow heating). Figure 5 allows to appreciate details which are characteristic for anisothermal TMF testing. Horizontal dotted reference lines are used in Figure 5 to indicate the positions of the maximum (σ_{MAX} - lowest temperature), mean (σ_{MEAN}) and minimum (σ_{MIN} - highest temperature) stresses in both cycles. Figure 5 shows that both cycles exhibit a positive mean stress, i.e. the absolute value of the saturation stress in tension (σ_{MAX}, lowest cycle temperature) is higher than in compression (σ_{MIN}, highest cycle temperature). The TMF conditions imposed in the present work result in very narrow stress-strain hysteresis loops. However, one can clearly see that the area of the loop for fast heating (cycle type 1) is smaller ($\oint \sigma d\varepsilon$ = 0.15 MJ/m^3) than for slow heating (cycle type 2), where more energy is dissipated ($\oint \sigma d\varepsilon$ = 0.43 MJ/m^3). In cycle type 1 (60 s heating followed by 30 s cooling), the tensile loading at 482 MPa and 1023 K causes a small positive plastic strain, which is not fully reversed in the compressive heating part of the cycle. In contrast, in cycle type 2 (300 s heating followed by 30 s cooling) we observe a significant accumulation of compressive plastic strain. This corresponds to a stronger relaxation of the compressive stress during slow heating than during fast heating (-344 MPa as compared to -425 MPa).

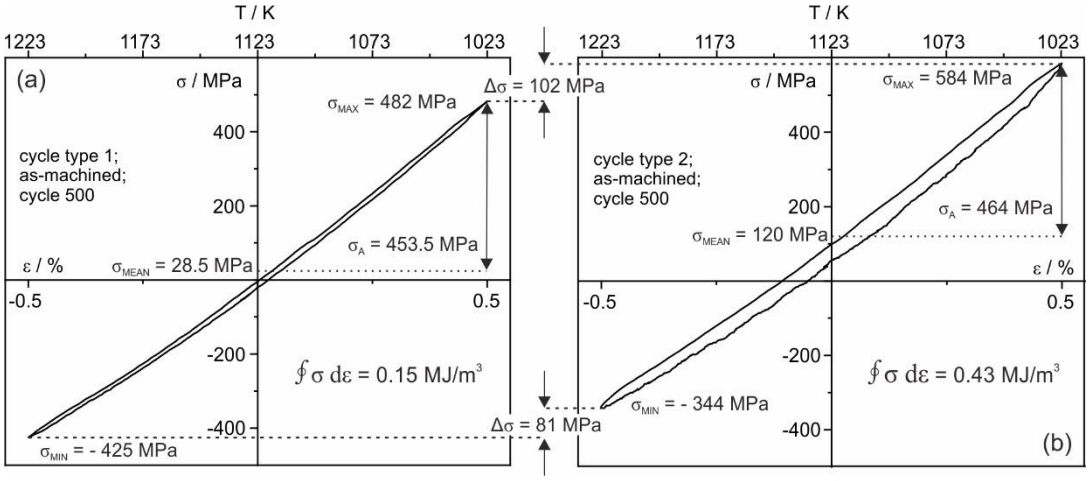

Figure 5: Stress-strain hysteresis loops after 500 cycles of the as-machined specimens for (a) cycle type 1 (specimen 5) and (b) cycle type 2 (specimen 6).

Figure 6 shows the stress-strain hysteresis loops of three tests after the 500th cycle (Figure 6 a to c) and the evolution of the maximum stresses σ_{MAX}, the mean stresses σ_{MEAN} and the minimum stresses σ_{MIN}, plotted as a function of the cycle number during the experiments. We compare the evolution of the maximum, mean and minimum stresses during cycling for specimen 1 (isothermal LCF test performed at the minimum temperature of the TMF test – 1023 K; represented by blue color), specimen 2 (isothermal LCF test performed at the maximum temperature of the TMF test – 1223 K; black color) and specimen 5 (TMF test with the same ε(t)-profile as the two isothermal tests; red color).

We keep in mind that in all cases total mechanical strains of ±0.5% were imposed and elongation/compression periods (from σ_{MIN} to σ_{MAX} and back) had durations of 30 and 60 s, respectively. It can be seen that the TMF test differs from the two isothermal tests. It exhibits the highest tensile stress and a positive mean stress unlike the isothermal tests. The TMF specimen (specimen 5) fails significantly earlier (N_f=2157) than the specimen tested isothermally at T_{max} (specimen 2, N_f=4072). The isothermal test performed at T_{min} (specimen 1) did still not fail after 20000 cycles, after which the test was interrupted.

Figure 7 summarizes the lifetime data of six fatigue experiments, failure lives (synonymous to numbers of cycles to failure) are plotted vs. specimen numbers (referring to the numbering of specimens introduced in Table 2). The left part of Figure 7a, shows that the TMF experiment performed with cycle type 1 exhibits a longer cyclic lifetime than the experiment performed imposing cycle type 2. The right part of Figure 7a documents lifetimes of the two isothermal experiments, which were performed in the program. As already evident from Fig. 6, both isothermal tests at 1223 K and 1023 K significantly outlive the two TMF-tests. The arrow in the isothermal 1023 K experiments indicates that the experiment was interrupted after 20000 cycles and the specimen did not fail. Figure 7b shows that no matter whether the surface is

rough (Figures 3a and c) or polished (Figures 3b and d), cycle type 1 conditions yield longer lifetimes than cycle type 2 conditions. Comparing the left and the right part of Figure 7b clearly shows, that polishing the surface of TMF specimens results in an increase of TMF-life by more than a factor of 2.

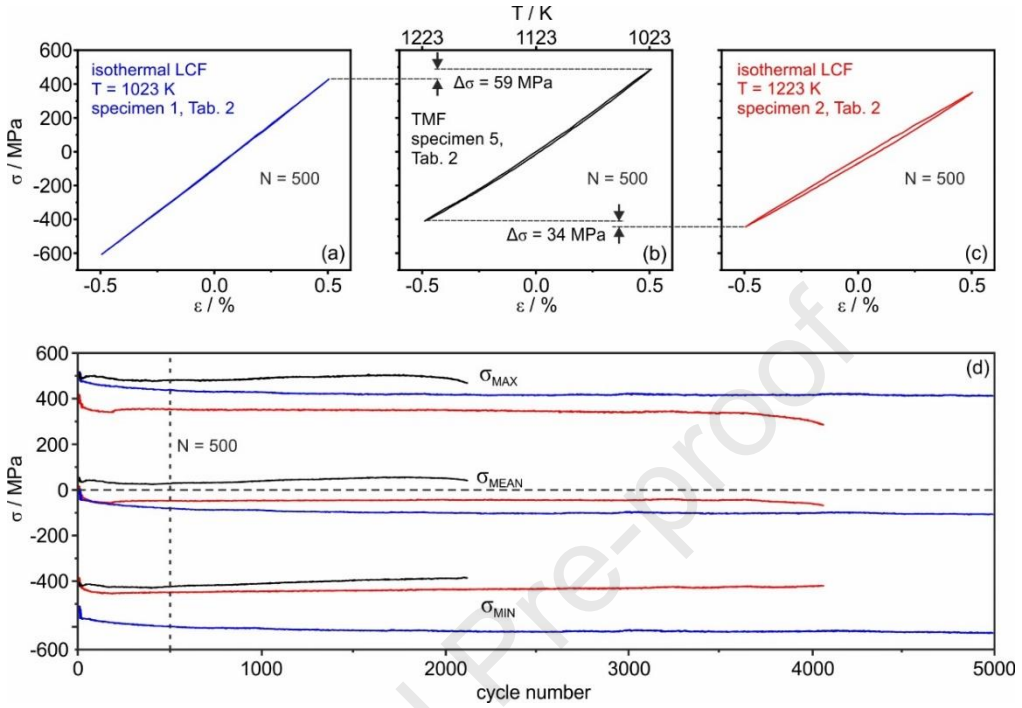

Figure 6: Cyclic stress-strain behavior during isothermal and thermomechanical fatigue loading. Stress-strain hysteresis loops after 500 cycles: (a) Isothermal LCF at 1023 K (specimen 1). (b) TMF test performed with cycle type 1 (specimen 5). (c) Isothermal LCF at 1223 K (specimen 2). (d) Evolution of σ_{MAX}, σ_{MEAN} and σ_{MIN} in fatigue tests 1 (blue curves), 2 (red curves) and 5 (black curves).

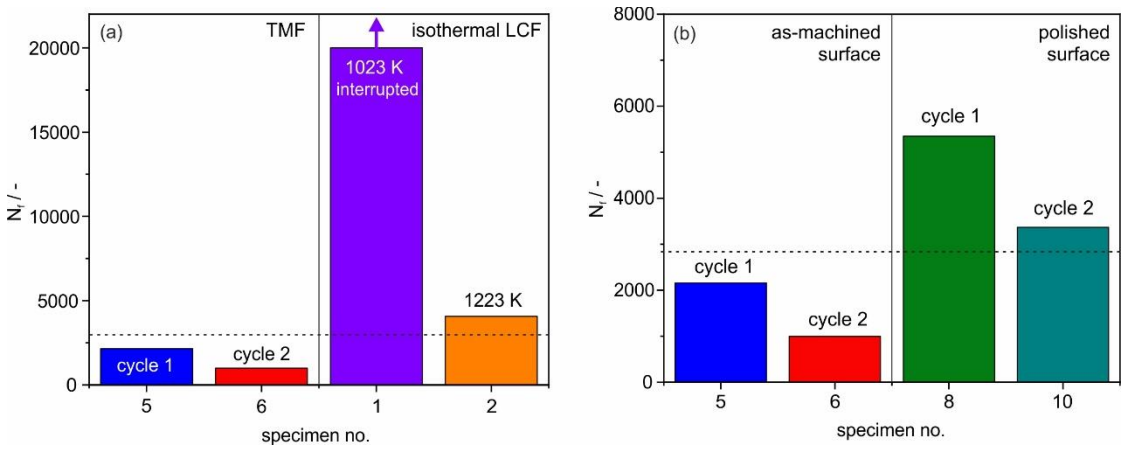

Figure 7: Comparison of number of cycles to fatigue failure. (a) On the left: Cycles to failure from TMF tests on as-machined specimens subjected to cycle types 1 and 2. On the right: Isothermal LCF tests performed at T_{max} and T_{min} temperatures applied in the TMF cycles. (b) On the left: Cycles to failure from TMF tests on as-machined specimens subjected to cycle types 1 and 2. On the right: Cycles to failure from TMF tests on polished specimens subjected to cycle types 1 and 2.

3.2 Evolution of surface features during TMF testing

Figure 8 shows three SEM micrographs which were taken from the surfaces of TMF-tested specimens in as-machined state. In all three micrographs, machining grooves which are perpendicular to the [001]-direction of the applied stress are clearly visible. Figures 8a and b show the surfaces of specimens which were subjected to TMF cycle type 1 and interrupted after 100 and 1000 cycles, respectively (specimens 3 and 4). Figure 8c shows the specimen which, under these conditions, ruptured after 2157 cycles (specimen 5). As can be seen in Figures 8a to c, machining grooves act as nucleation sites for small surface cracks. Many small surface cracks can be seen in Figure 8c.

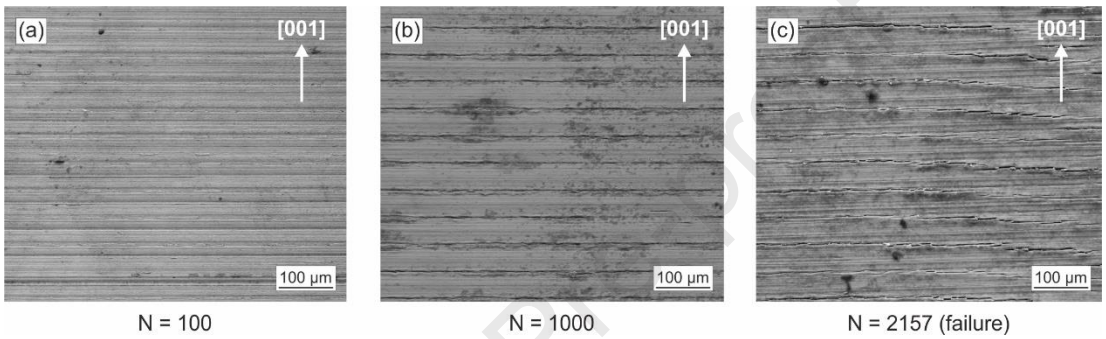

Figure 8: Formation of TMF surface cracks in the machining grooves of the specimen with the rough surface (RS, TMF cycle type 1). (a) 100 cycles (specimen 3). (b) 1000 cycles (specimen 4). (c) Failure after 2157 cycles (specimen 5).

The SEM images presented in Figure 9 were obtained from cross sections of the specimen 4 (cycle type 1, RS, 1000 TMF cycles, specimen 4, surface shown in Figure 8b). Figure 9 compiles four different SEM micrographs from the same region. For reference, two locations, a dark feature (in the center) and a crack-like feature (on the right) are highlighted by arrows.

Figure 9a presents a forward scattered electron micrograph (FSE contrast). Figure 9b displays the raw color-coded orientation information as an inverse pole figure (IPF), based on a conventional Hough indexation. Figure 9c presents color-coded orientation information. It consists of two parts. The pole figure in the upper left, first part of Figure 9c, defines the color-coding relative to a reference orientation, represented as the center of the pole figure. In the microstructure map, second part of Figure 9c (image), this reference orientation is established at the position marked by the cross on the left side. Finally, Figure 9d represents a kernel average misorientation (KAM) map, considering first order neighborhoods with no threshold angle. The KAM values are presented by colors as defined on the right of Figure 9d.

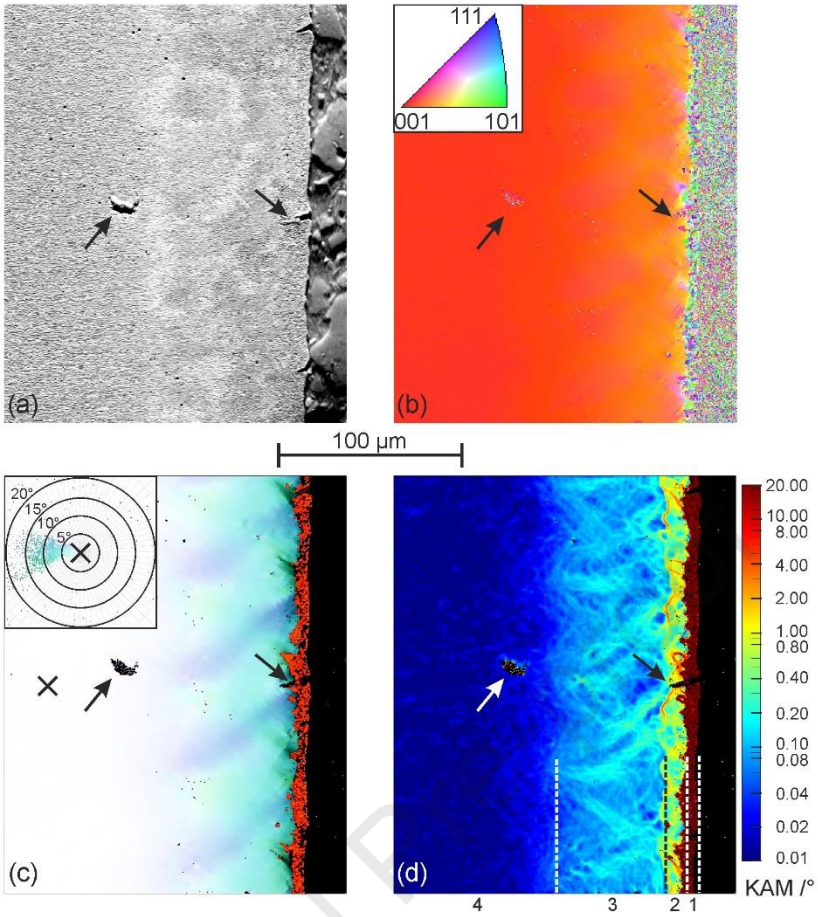

Figure 9: SEM results obtained for specimen 4 (TMF cycle type 1, RS, 1000 cycles). Individual color codes for b), c) and d) are presented within the subfigures. (a) Forward scattered electron (FSE) micrograph. (b) Conventional EBSD data visualized with a standard inverse pole figure (IPF) map cannot resolve the fine details, which characterize the surface region. (c) Misorientations relative to a reference orientation at a position marked with a cross visualized with a pole figure color-coding as indicated. High resolution RVB-EBSD data [49]. (d) High resolution Kernel Average Misorientation (KAM) map obtained from RVB-EBSD imaging.

The black area on the right represents the embedding material and is not considered. Then, moving inwards from the right to the left, four zones can be clearly distinguished, which are numbered from 1 to 4. Zone 1, with an average thickness of 8 µm, consists of fine grains shown in red. Zone 2, adjacent to this fine grain zone, exhibits an average thickness of 12 µm and features locally deformed regions emanating from surface cracks and other zone 1 protrusions, with KAM values exceeding 2°. Zone 3 has a thickness of 60 µm. It can be clearly distinguished from the bulk material in zone 4, which appears in dark blue. In Figures 9c and d, zone 3 exhibits regular deformation patterns. These correspond to localized deformation bands, with a spacing of the order of 50 µm. They are associated with local misorientations of the order of 15° at the interface between zones 2 and 1. Figure 9d reveals, that there is a grid-like fine-scale deformation substructure, which corresponds to KAM values of 0.2°. In the cross section on the right, one can see shear bands, which have formed in 45° to the direction of the applied stress. They have formed all along the gauge length section considered.

In Figure 10 we show the surface of specimen 10 (PS, cycle type 2), where failure occurred after 3365 cycles. The total test duration was 308 hours. Figure 10a shows long features parallel to the [001] loading direction. Their spacing is of the order of 500 µm, which is close to the average dendrite spacing in our material [47]. EDX line scan analysis was performed in the region highlighted with a black dashed rectangle in Figure 9a. The results for O, Cr and Al are shown in Figure 9b. It can be seen that the oxide layers which form on the surfaces of dendritic (light grey) and interdendritic regions (dark grey) differ in Cr and Al content. Interdendritic regions contain a little more Al and less Cr than dendritic regions. Small surface cracks have formed perpendicular to the direction of the applied stress, even in the absence of the machining grooves. The features of these cracks seem not to be affected by their location in the cast microstructure, e.g. whether they are located in dendritic or interdendritic regions.

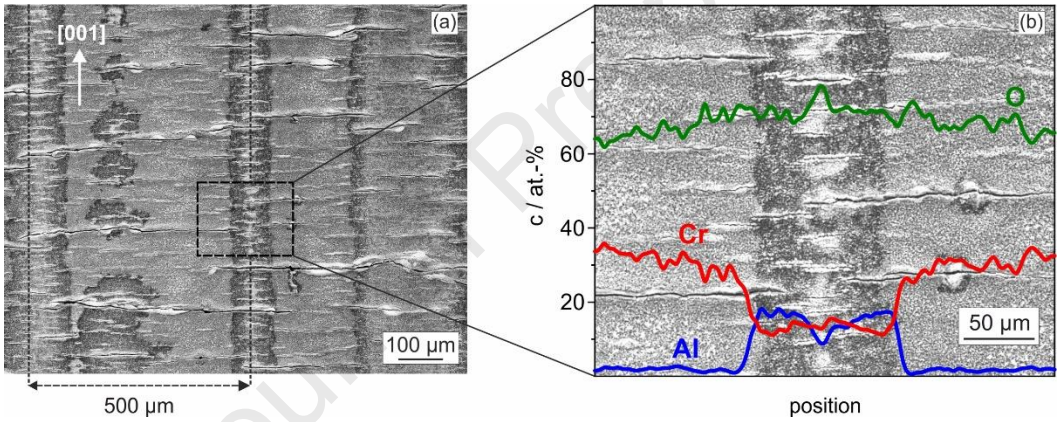

Figure 10: Small surface TMF cracks which have formed perpendicular to the applied stress in the surface of a polished specimen subjected to TMF cycle type 2 (specimen 10, TMF failure occurred after 3365 cycles). (a) Longitudinal features are associated with the dendritic microstructure, for details see text. (b) A line scan performed in the region highlighted with a dashed rectangle in Figure 10a, across an interdendritic region, reveals a change in local Al and Cr concentration.

An effort was made to measure the length distributions of the small cracks, which form perpendicular to the direction of the applied stress in polished specimens subjected to TMF cycles of type 1 and 2 after rupture (specimens 8 and 10). Figure 11a and b show overview SEM micrographs, images taken with higher magnifications are shown in Figures 11c and d. White rectangles in Figures 11c and d highlight a smaller (36 µm in Figure 11c) and a larger (235 µm in Figure 11d) circumferential crack. In both specimens, almost 800 crack lengths were measured. Their length distributions are presented as histograms in Figures 11e and f. Cycle type 1 loading (mean crack length: 102 µm) results in significantly less small cracks then cycle type 2 loading (mean crack length: 88 µm). The data presented in the two histograms of Figures 11e and f do not allow to conclude that cycle type 2 conditions which result in shorter TMF rupture lives are associated with larger circumferential surface cracks.

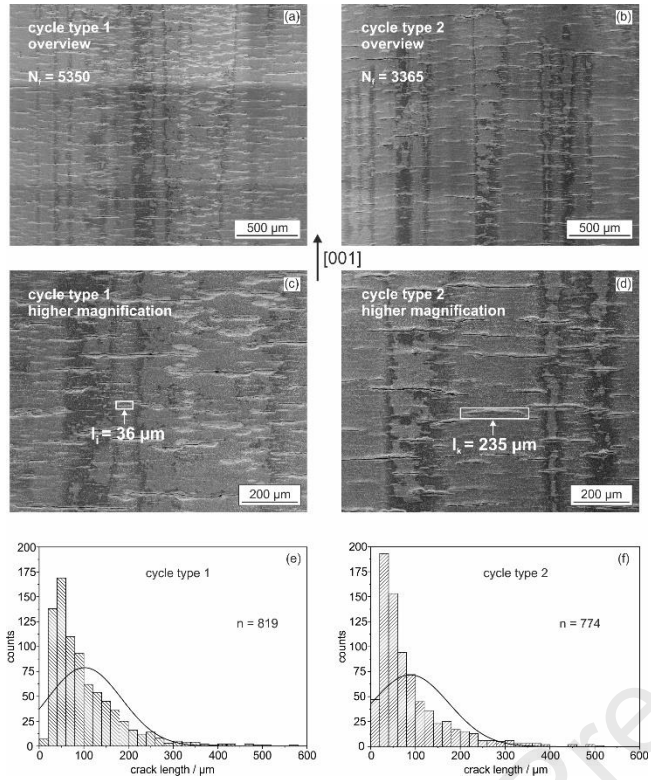

Figure 11: Surface cracks which have formed in failed specimens. (a) - (d): SEM micrographs of specimen surface after TMF fatigue loading. (e), (f): Distribution of lengths of circumferential surface cracks after TMF failure. (a) and (c): SEM micrographs of polished surfaces subjected to TMF cycle type 1 at lower and higher magnifications (specimen 8). (b) and (d): SEM micrographs of polished surfaces subjected to TMF cycle type 2 at lower and higher magnifications (specimen 10).

3.3 TMF cracks

Figure 12 shows cross sections of two specimens with polished surfaces, which were cycled through to failure (specimens 8 and 1). The cross section in Figure 12a was obtained from the specimen subjected to cycle type 1, where TMF failure occurred after 5350 cycles. The cross section shown in Figure 12b derives from the specimen subjected to cycle type 2, where failure occurred earlier, after 3365 cycles. In both cases, one can see 7 larger cracks which have formed in a gauge length section of 500 µm (average distance: 71 µm). The cracks have grown perpendicular to the [001] loading direction. The lengths of all macro cracks are attributed to 5 size classes in the histogram of Figure 12c. It can be seen that cycle type 2, which shows the shorter cyclic failure life, has led to the formation of two cracks in the largest size class, while only one crack of this size is found for cycle type 1. It must be kept in mind, that none of the cracks shown in Figures 12a and b was responsible for final failure. Figure 12b shows slip traces of local deformation events of the type, which has been reported by Moverare et al. [29]. The macroscopic slip lines have a similar spacing as the macro cracks. While they account for the overall plastic deformation, the micrograph in Figure 12b suggests that they are not correlated with the macro cracks. Most importantly, the macro cracks neither nucleate at these slip lines nor grow along these slip bands, Figure 12b.

A SEM micrograph of the fracture surface of the specimen subjected to cycle type 1 (specimen 8, PS, N_f = 5350) is shown in Figure 13a. One can clearly identify the initiation site of the principal crack which has caused the failure. In case of the specimen which was subjected to cycle type 2 (specimen 10, PS, N_f = 3365), failure manifested itself by a complete loss of tensile

resistance. The two parts of the specimen were not yet fully separated. Figure 13b shows the principal crack on the specimen surface. Its size of several millimeters (>3 mm in Figure 13b) by far exceeds the sizes of the circumferential surface cracks shown in Figures 11b and d (only very few cracks exhibit sizes close to 0.5 mm).

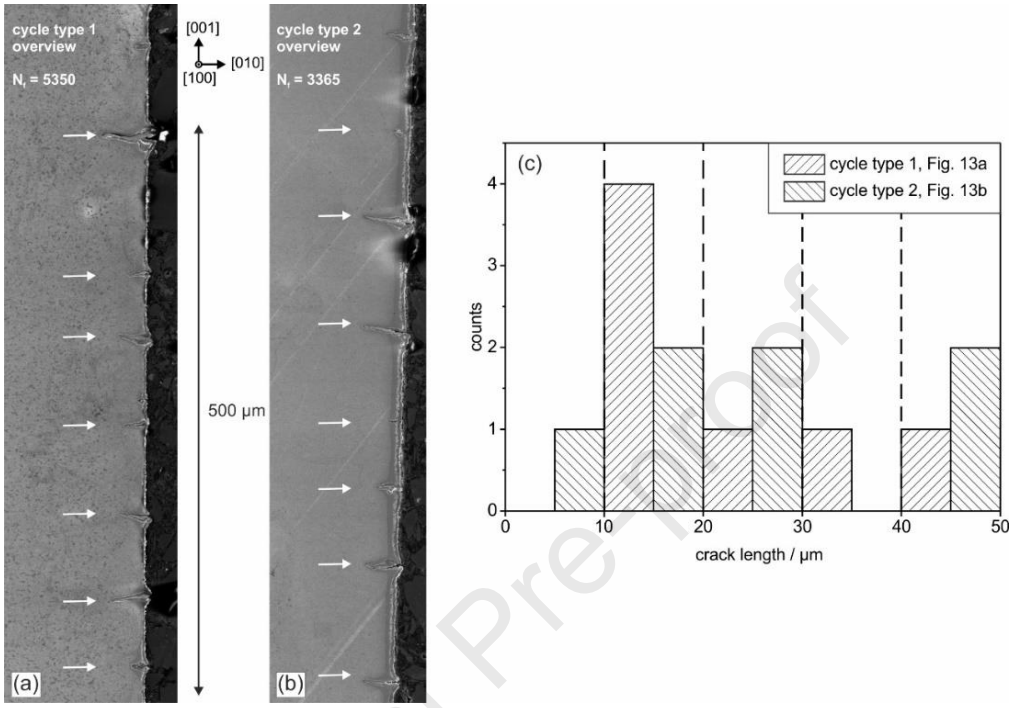

Figure 12: SEM results from metallographic longitudinal cross sections of originally polished TMF-specimens which were cycled through to failure. (a) Specimen 8 (cycle type 1). (b) Specimen 10 (cycle type 2). (c) Histogram showing the distribution of the few observed cracks. For details see text.

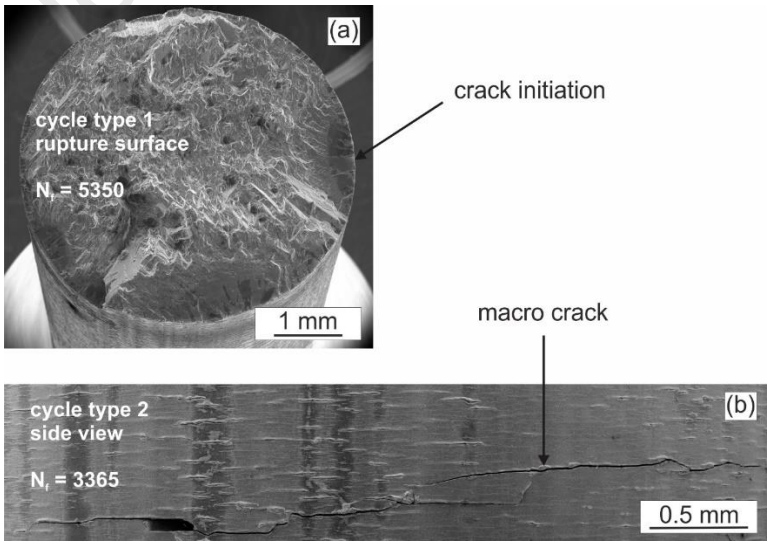

Figure 13: SEM micrographs taken from originally polished TMF-specimens (specimens 8 and 10) after rupture. (a) Rupture surface of specimen subjected to cycle type 1. The initiation site of the crack, which led to final rupture is indicated by an arrow. (b) Specimen surface of specimen subjected to cycle type 2 after complete loss of tensile resistance. Circumferential macro crack associated with end of TMF-life extends over several millimeters.

3.4 Oxide scale growth

In Figure 14 we analyze one macrocrack, which has formed under cycle type 2 conditions during 1000 TMF cycles in more detail (specimen 9). In the upper SEM micrograph the position of the crack tip on the very left is marked by a vertical dashed line marked with 0. For the following we make two first order assumptions. First, we assume the crack is initiated in cycle 1. Second, the crack propagates by the same amount in each of the 1000 TMF cycles, i.e. the crack propagation rate is constant. We acknowledge that this needs to be considered with care since fatigue crack propagation rates can depend on the crack length. However, the overall crack length of about 100 µm is relatively short and the crack growth is heavily influenced by time-dependent oxidation processes. Therefore, we assume that under the conditions of the present work the crack propagation rate does not strongly depend on the crack. The assumption of a constant crack growth rate allows to subdivide the crack length into 10 intervals, each of which corresponds to 100 cycles of crack growth. The vertical dashed lines marked from 0 to 9 show the corresponding locations. This subdivision allows to obtain information on which part of the crack has evolved in how many cycles. For example, the crack tip region between 1 and 0 has grown during 100 cycles, between 4 and 0, crack extension occurred during 400 cycles and so on.

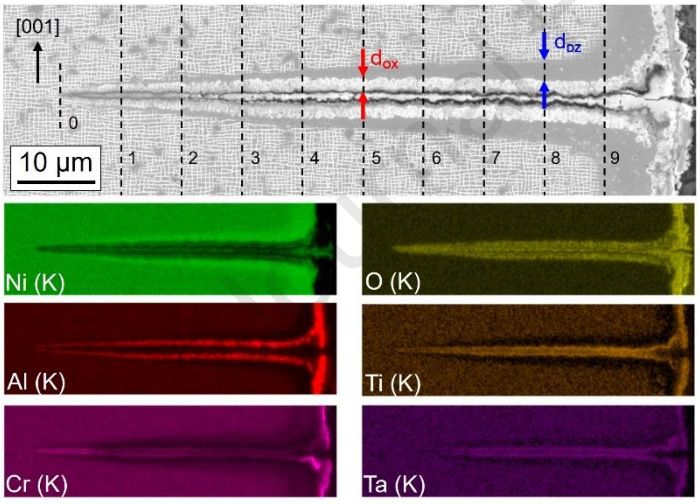

Figure 14: Macro crack which has formed during 1000 TMF cycles (cycle type 2, specimen 9). Upper SEM micrograph documents how thicknesses of the oxide layer d_{OX} and of the γ'-depleted zone d_{DZ} were measured. The colored images show element distribution maps and document enrichment / depletion of Al, Ti, Cr and Ta in the oxide layer / depleted zone.

The upper SEM image in Figure 14 allows to distinguish the γ/γ'-microstructure of the bulk material. At the crack flanks and at the specimen surface one can distinguish an inner γ'-depleted zone (DZ) of thickness d_{DZ} (marked with a blue double arrow at position 8) and an outer oxide layer of thickness d_{OX} (marked with a red double arrow at position 5). It can be clearly seen that the thicknesses of these reaction zones change along the crack length. The EDX element distribution maps in Figure 14 show that the subsurface layer exhibit lower concentrations of oxide-forming elements such as Cr, Ti, Ta and Al which are enriched in the outer oxide layer. The outward diffusion of these elements leads to the formation of a γ'-depleted zone.

Thicknesses of the reaction layers were measured on the specimen surface and along the crack at 9 different positions. For the reaction layers along the crack flank, the average of two measurements conducted on both sides of the crack (above and below) is plotted in Figure 15. Figures 15a and b show how the thicknesses of the oxide scale d_{OX} and the thickness of the depleted zone d_{DZ} vary along the crack flanks, as a function of the distance x from the crack tip (oxide layer: circles in Figure 15a; depleted zone: squares in Figure 15b; empty symbols: measurements along crack flank; full symbols: measurements on specimen surface not affected by the presence of macro crack). Figure 15a shows that the thickness of the oxide scale increases along the crack flank, until the oxide layer reaches a thickness of 2 µm and stays afterwards constant. A vertical dashed line marks the transition from increasing to constant oxide thickness. The thickness of the depleted zone increases along the whole crack length, Figure 15b. Its increase is even stronger in the region where the oxide thickness no longer changes.

The plots in Figure 15c and d were obtained, assuming that significant oxidation only occurs at temperatures above 1173 K. This temperature threshold was based on the authors' own experience (negligible oxidation in laboratory time scales during creep testing 1123 K [54]) and on kinetic data published in [58,59]. Sato et al. [58] and Pistor et al. [59] consider transforming appropriately chosen weight gain parabolic rate constants k_w into layer growth parabolic rate constant k_x by dividing k_w by ρ ($k_x=k_w/\rho$), where ρ was taken as 4 g/cm^3, a value which is close to the densities of Al_2O_3 and TiO_2. In each cycle of cycle type 2 (slow heating), a time interval of 82.5 s is spent above 1123 K, in the compressive part of the cycle. It is then straightforward to obtain the exposure times spent above this temperature at the different locations marked in Figure 14. In Figures 15c and d we plot the thickness results presented in Figures 15a and b as a function of the square root of these exposure times.

Figures 14 and 15 also show that the thickness of the oxide layer at the specimen surface, which is not affected by the presence of the macro crack is significantly thicker than one would expect from the thickness data acquired along the crack.

Figures 16a and b show SEM micrographs, which were obtained after isothermal fatigue testing (specimens 1 and 2). Only a few small cracks can be observed along the gauge length overview montage in Figure 16a, left. The higher magnification micrograph on the right of Figure 16a (1023 K) allows to distinguish cuboidal γ'-particles. The outer oxide layer has a thickness of 0.2 µm. At the higher temperature of 1223 K, an oxide layer of 1 µm thickness is observed and an extended γ'-depleted zone (width: up to several µm) has formed, Figure 16b. It is noteworthy that the high magnification SEM micrograph in Figure 16a shows a cast micro pore close to the surface. Its stress field appears to have affected the evolution of the γ/γ'-microstructure in its vicinity. However, this micro pore did not assist in the nucleation of a LCF surface crack, a mechanism, which has been observed for the single crystal superalloy AM1 [21] and CMSX-4 [25]. It is noteworthy that the oxide layer of the high temperature LCF test at 1273 K in Figure 16b is also significantly thinner than observed in the OP-TMF test in Figures

14 and 15. The overview montage along the gauge length of the LCF specimen shows more small cracks than in case of the 1023 K experiment.

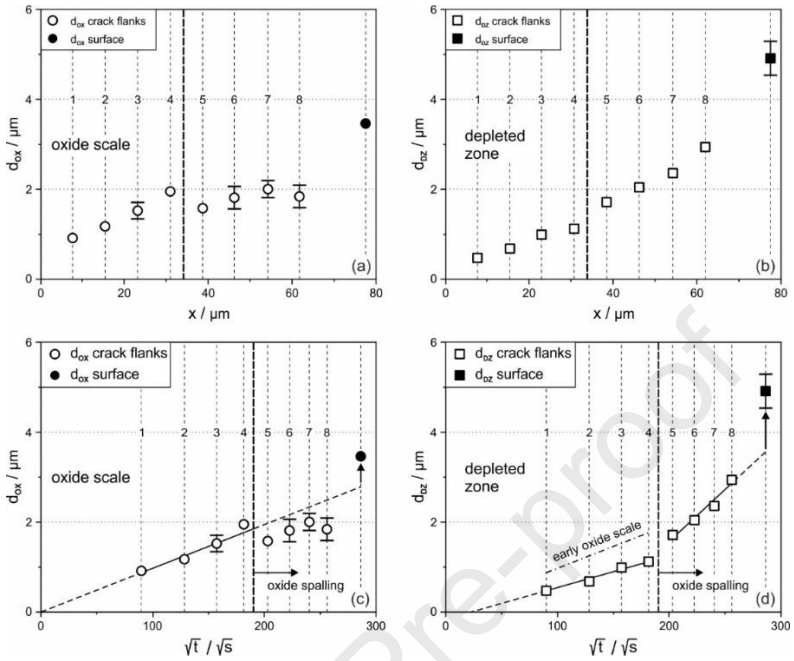

Figure 15: Thicknesses of oxide layer d_{OX} and depleted zone d_{DZ} along crack length. (a, b) Direct measurements along the crack. (c, d) Associating locations along crack with exposure times and interpreting data in terms of a parabolic rate law. (a, c) Oxide scale thicknesses. (b, d) Thicknesses of depleted zone.

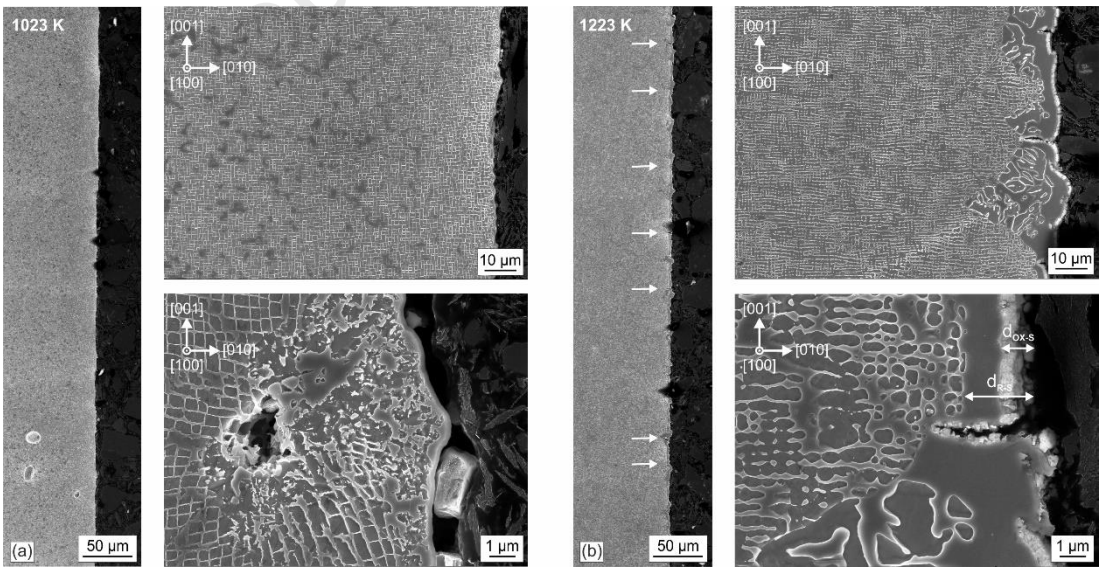

Figure 16: SEM micrographs of cross sections of surface regions after isothermal fatigue testing of specimens with rough surfaces. (a) Specimen 1 (interrupted after 20000 cycles at 1023 K): oxide layer thickness = 0.2 µm, cast micro pore close to surface does not assist in crack formation. (b) Specimen 2 (rupture after 4072 cycles): oxide layer thickness = 1.0 µm, significant coarsening of γ/γ'-microstructure) in the environment of small surface crack.

Table 3 summarizes the average thicknesses of the reaction layers on specimen surface regions, which were not affected by the presence of a macrocrack, for the isothermal LCF experiments performed at 1023 (interrupted after 20000 cycles, exposure time: 500 h) and 1223 K (failed after 4072 cycles, exposure time: 102 h) and for the OP-TMF experiment 9 (interrupted after 1000 cycles, exposure time: 92 h).

Table 3: Thicknesses of reaction layers on specimen surfaces, which have formed under OP-TMF and isothermal LCF conditions.

Test	Reference no. (Table 2)	SEM micrograph	Depleted zone thickness / µm	Oxide layer thickness / µm
Isothermal LCF 1023 K	1	Fig. 16a	<0.1	0.2
Isothermal LCF 1223 K	2	Fig. 16b	1.7	1.0
OP-TMF 1023-1223 K	9	Figs. 14 and 15	4.6	3.4

4. Discussion

4.1 General findings

The present work was performed on precisely oriented [001] specimens. This allows to exclude experimental scatter associated with crystallographic orientation, associated with the anisotropy of elastic constants [60] and of high temperature plasticity [52,54]. The present work confirms two well accepted findings.

First, rougher specimen surfaces result in shorter cyclic lives, Figures 3 and 7b. Since fatigue cracks initiate predominantly at the specimen surface, this is expected for all types of fatigue loading [12]. The importance of the surface condition on fatigue lives of superalloys is well appreciated [34,35,37]. Figure 8 suggests that short crack growth starts in each machining groove. The frequency of these surface cracks does not differ between dendritic and interdendritic surface regions, where average alloy compositions differ, Figure 10. Many small circumferential surface cracks can be found after failure, Figure 11. The surface crack length distributions of small cracks which form in the OP-TMF specimens with longer (N_f = 5350, cycle type 1) and shorter (N_f = 3365, cycle type 2) cyclic failure lives do not differ significantly, Figure 11. Only a few of the small circumferential cracks evolve into macro cracks, like those shown in Figure 12 and 16. Only one of these cracks outgrows all the others and eventually causes final failure, Figure 13. Hence, given the early fatigue crack initiation due to cracking of brittle surface oxides under relatively high tensile stress at low temperatures, OP-TMF life of ERBO/1 within 1023 to 1223 K is determined by the resistance to the growth of the principal fatigue crack.

Second, isothermal fatigue tests performed at the highest and lowest temperature of an OP-TMF test, cannot predict the cyclic failure life of the OP-TMF test. The stress-strain hysteresis loops in Figure 6 recorded after cycle number 500 show that there is a mechanical reason for this finding. The stress-strain hysteresis loop of the OP-TMF test differs from the two isothermal tests in a positive mean stress of the stress-strain cycle and featuring the highest tensile stress at 1023 K. Both factors promote crack growth and thus earlier fatigue failure. Furthermore, under OP-TMP loading conditions, oxide layers forming at high temperature under compressive stress can easily crack under tensile stress at lower temperatures, when they exhibit low ductility. This mechanism forms sharp and fast cracks seamed by oxide layers as shown in Figure 14, which are typical for OP-TMF loading [30]. Under isothermal loading at 1023 K, no pronounced oxide layer forms while at 1223 K, the oxide layer is more ductile preventing brittle cracking (Figure 16). Thus, only OP-TMF loading provides the conditions to form sharp oxidized cracks, which contributes to lower lifetimes when compared to isothermal loading. The finding that isothermal LCF tests cannot mimic the rupture behavior observed in OP-TMF tests has been reported in previous studies [24,28,30].

In the present work, the microstructural evolution in the surface regions of OP-TMF specimens 4 and 10 was studied, Figures 9 and 12b. In specimen 4, a narrow zone of recrystallized nanograins was found at the surface, Figures 9b to d. Moving inwards, a second narrow deformation zone has developed. These two zones are not observed in case of the polished specimen 10, Figure 12b. In both specimens, localized deformation bands are found. The small crack marked with a black arrow in Figures 9c and d does not appear to follow the localized deformation bands. From Figure 12b it is clear that under the present OP-TMF conditions, macro cracks do not follow the localized deformation bands. Moverare et al. [29], Hong et al [30] and Guth et al. [33], who studied OP-TMF of CMSX-4 and Alloy 247 LC DS, respectively, found similar deformation bands, which were identified as deformation twins. In their cases, cracks tended to follow the twins and in [29] topologically closed packed (TCP) phases precipitated along the twins are reported, which is in contrast to our results. This might be due to different TMF temperature ranges. All above mentioned studies applied lower minimum temperatures (between 373 and 673 K) than in this study, indicating that cracking along deformation twins occurs under tensile load at lower temperatures than tested here. Moverare et al. [29] used higher maximum temperature of 1273 K along with longer cycle times of 777 s, which may be a requirement for precipitation of TCP phases. Meid et al. [36] studied isothermal LCF of ERBO/1 at 1223 K and found precipitation of TCP phases, which interact with propagating cracks. This supports the assumption that the TMF conditions applied here do not provide sufficient time at temperatures ≥1223 K to precipitate TCP phases. Hong et al. [30] studied OP-TMF of CMSX-4 applying a similar strain range but shorter cycle times. They applied the same maximum temperature than in our case while they used a lower minimum temperature of 673 K. They provide excellent microstructural information, showing that localized deformation bands identified as twins can emanate from cracks tips, once these have reached a certain length. This was not observed for the test conditions applied in the present work, which may again be due to different minimum temperatures. It

can be concluded that for the OP-TMF conditions tested here with the relatively high minimal temperature, deformation twinning and cracking are not correlated. In the surface region of the OP-TMF specimen with an originally rough surface subjected to 1000 cycles under cycle type 1 conditions (specimen 4), one finds localized deformation bands with an average spacing of 50 µm, Figures 9c and d.

A characteristic feature of the surface regions shown in Figures 12a and b (specimens 8 and 10; PS; cycle types 1 and 2, respectively) is the presence of a regular array of macro cracks, with an average spacing of 71 µm. The localized deformation bands also form a regular array in Figure 12b and exhibit a similar average spacing of 50 µm. Such bands, which likely represent deformation twins as observed in [30], can also be seen in Figure 12b after rupture which occurred after 3365 OP-TMF cycles in a specimen with an originally polished surface subjected to cycle type 2 (specimen 10). These bands are not necessarily associated with macro cracks, Figure 12b. Both surface features, cracks and localized deformation bands, nucleate and grow under OP-TMF conditions. However, for the alloy investigated under the mild OP-TMF conditions applied in the present study (relatively high T_{min} levels as compared to other studies) cracks and shear bands are not correlated, neither on the micro nor on the macro scale, Figures 9 and 12. Figures 9 and 12 show that microscopic and macroscopic cracks and localized shear bands are not correlated. This suggests, that crack nucleation occurs in the brittle oxide scale, which does not deform plastically. Once a crack has nucleated in the oxide scale, it grows into the alloy, driven by the highest crack driving force, related to the stress intensity factor K_I, which promotes crack growth perpendicular to the direction of the applied tensile stress.

4.2 TMF cycle shape

It was shown that cycle type 2, where a longer time period is spent in the compression/heating part of the OP-TMF cycle (300 s as compared to 60 s in cycle type 1), results in shorter TMF lives, Figure 7. In Figure 17 we interpret the mechanical results shown in the hysteresis loops of Figure 5. The initial state, where no mechanical strain is imposed ($\varepsilon_{tot} = 0$), is shown on the left. A schematic thermometer indicates the temperature (blue: 1023 K – cold, red: 1223 K – hot). The horizontal dashed lines indicate three positions of the total mechanical strain, which varies between -0.5 and +0.5% total mechanical strain. The total mechanical strain has elastic and plastic parts, which are represented by a spring and a dashpot. The cycle starts with its compressive part when a total mechanical strain of -0.5% is imposed. It can be seen that the faster heating in cycle type 1 results in less compressive deformation of the dashpot than slower heating in cycle type 2. This corresponds to lower minimum stresses in cycle type 2 as shown in Figure 5. As schematically illustrated on the right, moving from -0.5 to +0.5% total strain results in a higher extension of the spring representing cycle type two, because the higher accumulated strain of the dashpot in compression has to be compensated. The longer spring in our simple model corresponds to a higher stress in the cold tensile part of experiments performed under cycle type 2. Hence, more compressive creep causes higher elastic stresses in the subsequent tensile part of the cycle. This is one reason why cycle type 2

(more accumulation of plastic strain in compression, subsequently higher elastic stresses in tension) shows lower rupture lives (3365 cycles as compared to 5350 cycles in cycle type 1). Higher tensile stresses result in higher crack propagation rates. Hence, slower heating rates under OP-TMF loading reduce the lifetime by an indirect creep effect, which is not associated with microstructural creep damage, but with plastic strain accumulation as discussed. It must also be considered, that the total OP-TMF exposure time of cycle type 2, with the lower cyclic life (3365 cycles to failure) is 308.5 h. A significantly smaller exposure time of 133.8 h is spent during the accumulation of 5350 cycles to failure during cycle type 1.

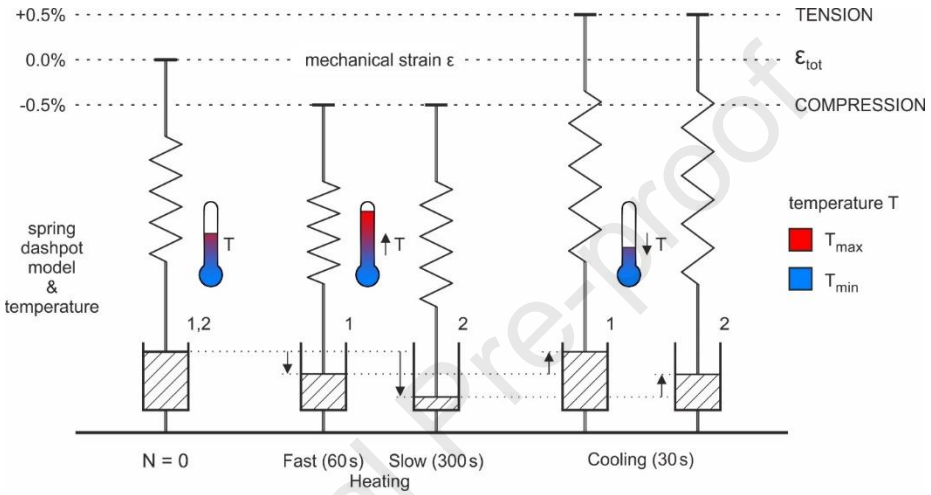

Figure 17: Simple spring dashpot model illustrating why lower heating rates in the compressive part of the cycle with peak temperature T_{max} lead to higher stresses in the subsequent tensile part of the cycle.

The slower heating part of cycle type 2 is associated with a higher accumulation of plastic strain, and thus compressive creep is more pronounced in cycle type 2 than in cycle type 1. The results of the present work show that this stronger compressive creep part of the TMF cycle 2 indirectly shortens the lifetime. This is not a microstructural type of creep fatigue interaction, where for example creep cavities accelerate fatigue crack growth [e.g. 61,62]. Instead, the more pronounced compressive creep strain accumulation in cycle type 2 (slow heating) makes it more difficult to impose 0.5% mechanical strain in the subsequent tensile part of the cycle. Slower heating in the compressive part of the OP-TMF cycle results in dynamic recovery (dislocation annihilation occurs during high temperature deformation), which is associated with lower compressive peak stresses. This finding is in good qualitative agreement with previous work, where strain-controlled compression holds were considered in OP-TMF testing, where recovery is of a static nature (dislocations annihilate without the accumulation of macroscopic plastic strain) and stress relaxation occurs during compression holds [29]. Strain-controlled compression holds at the maximum temperature of OP-TMF cycles also typically result in a shortening of cyclic lives. This was reported in two recent publications for polycrystalline Ni-base superalloys [40,41] (Inconel 713LC, 773-1173 K, ±0.3%, compression hold time: 600 s [40]; DS alloy of CM 247 LC type, 723-1123 K, ±0.55-0.8%, compression hold time: 300 s [41]). It had also been previously reported for the single crystal Ni-base superalloys TMS-75 and TMS-82+ [42] (673-1173 K, ±1.28% and ±1.27%, hold time:

600 s) and for CMSX-4 [43] (673-1273 K, ±0.7-1.1%, hold time: 300 s). All tests have in common, that recovery in the compressive high temperature part of an OP-TMF cycle relaxes stresses by transforming elastic into plastic strain. Higher stresses are required in the low temperature tensile part of the cycle, to establish the mechanical strain level which characterizes the OP-TMF test. Lowering the minimum temperature has been shown to further reduce OP-TMF lives [43].

4.3 Oxidation phenomena

Since the seminal work of Rémy and his group [16,17,21,22] and Wright [18] it was clear that oxidation represented a central element of high temperature fatigue crack initiation and growth. Reuchet and Rémy [16] suggested to explicitly consider the contributions of two factors, mechanical loading and oxidation to high temperature fatigue damage accumulation. Wright [18] showed that one observes longer fatigue lives at lower oxygen partial pressures, a fact which also applies to material classes with distinctly different bulk microstructures, like for example tempered martensite ferritic steels [63]. Earlier works [16,17,18,21,22,63] have shown that fatigue cracking starts with crack initiation on the specimen surface and that it is affected by the test environment.

The observations in the present work regarding the oxidation of the flanks of a TMF crack in Figure 14 are remarkable. Based on the assumptions and following the procedure outlined in section 3.4, one can associate crack locations with exposure times. In Figures 15c and d, the oxide thicknesses d_{OX} and the thickness of the underlying depleted zone d_{DZ} are plotted against the square root of these time values. The fact that one obtains straight lines suggests that the growth of both layers is diffusion-controlled. The fact that metal oxidation is diffusion-controlled is known since the seminal work of C. Wagner on the reaction of copper with oxygen, who could rationalize the parabolic rate constant on the basis of the mobility of ions diffusing through anion vacancies in the growing oxide lattice [64]. Oxide growth of engineering alloys is more complex [58,59,65,66]. But diffusion-controlled oxide growth with parabolic growth for single crystal superalloys has been reported earlier [58,59].

The EDX element distribution maps in Figure 14 show that oxide forming elements like Al, Cr, Ta and Ti diffuse to the surface where they react with oxygen.

The results for the oxide growth in Figure 15c, where oxide layer thickness grows governed by a parabolic rate law, suggest that early oxidation along the crack flanks is diffusion-controlled. This also holds for the early growth of the depleted zone shown in Figure 15d. It must be kept in mind, that under our OP-TMF conditions the oxide growth occurs mostly in the compressive part of the cycle. The fact that the oxide does not grow further after it has reached a thickness of 2 µm, is associated with mechanically enforced spalling processes, Figure 15c. It seems reasonable to assume, that thin oxide layers (<2 µm, Figures 14 and 15) can withstand high compressive loads in the crack closure periods during the high temperature compressive parts of the cycle. The fact that oxide thicknesses >2 µm are not observed along the crack flanks suggests, that thicker oxides suffer cracking and spallation processes.

Note that the growth rate of the depleted zone increases, after the oxide thickness has reached a constant value. From a reaction kinetics point of view, oxide layer growth and depleted zone layer growth are coupled and represent consecutive reactions. First, alloy elements must diffuse to the surface, so that the oxide can grow. The short-term results in Figures 15c and d show that initially, the increase of the layer thicknesses occurs at a similar rate. After the onset of oxide spalling, the growth rate of the depleted zone increases. This suggests that the diffusion processes, which govern oxide growth are slower than those, which characterize the mobility of alloy atoms in the depleted zone. In the early stages, the oxide growth is rate-controlling. The fact that the depleted zone keeps growing once the oxide layer has established a constant thickness shows that oxidation does continue, but mechanical spalling continuously removes reaction products. Under this condition, the growth of the depleted zone is no longer constrained by the diffusion-controlled growth of the oxide. The results presented in Figures 14 and 15 also show, that the oxide which has formed on the specimen surface in a region which is not affected by the presence of the macro crack is significantly thicker than one would predict by extrapolating the crack flank oxide growth data. It must be kept mind that the oxide growth on the crack flank occurs under a compressive stress, which does not suppress diffusion of oxygen into the closed crack but slows it down. This can explain the difference between stress-free oxide growth on the surface and oxide growth under compressive stresses at the crack flanks.

There is another observation, which is not intuitive. Oxide layers, which form during the two isothermal fatigue tests in Figures 16a and b are significantly thinner than the layer which formed under OP-TMF conditions, Figure 14. This is not unexpected for the isothermal LCF test performed at the lower temperature of 1023 K. On first sight it seems surprising, however, that this is also observed for the isothermal LCF test performed at the higher temperature of 1223 K.

It has been reported that oxidation attack is faster when temperatures are cycled than under isothermal conditions [67-69]. Hebsur and Miner [67] have studied the Ni-base superalloy PWA1480. They used weight gain studies to compare isothermal oxidation at temperatures between 1323 and 1473 K (where Cr_2O_3 becomes volatile [67] and where the γ'-volume fraction decreases below 56% [70]). Smialek [68] and Poquillon and Monceau [69] rationalize faster oxidation attack by spalling models, which assume that oxide scale spalling continuously accompanies oxide growth. The fact that the thick oxide layer after 1000 TMF cycles in Figure 14 shows no signs of spalling suggests, that there are other factors than spalling which account for faster oxide growth under cyclic oxidation conditions. Further work is required to clarify this point.

5. Summary and Conclusions

In the present work the out-of-phase thermomechanical fatigue (OP-TMF) behavior of [001]-oriented single crystal Ni-base superalloy ERBO/1 (CMSX-4 type) specimens were studied. Total mechanical strains were cycled between -0.5 and +0.5% while the temperature simultaneously varied from 1223 to 1023 K. Two cycle types were considered which differed in the compressive/heating part of the cycle (fast and slow heating). For reference, isothermal LCF tests were performed at 1023 and 1223 K. From the results, the following conclusions can be drawn:

(1) The present work provides further evidence for well-established high temperature LCF findings. Thus, specimens with rough surfaces fail earlier than specimens with polished surfaces and OP-TMF loading results in lower lifetimes than isothermal LCF loading. Hence, cyclic OP-TMF lives cannot be predicted based on isothermal LCF tests alone.

(2) In specimen with rough surfaces, a small zone of recrystallized nanograins forms below the surface and the presence of many circumferential micro cracks characterizes the specimen surface. Local deformation bands, which are likely to be twins, were also observed at the specimen surface. None of these features led to precipitation of new phases or could be directly associated with crack initiation or growth.

(3) Slower heating under OP-TMF conditions results in increased compressive creep deformation. In the following tensile part of the cycle, higher stress is required to pull the specimen to maximum strain. The higher stresses increase crack propagation rates and thus lead to lower lifetimes for slower heating rates.

(4) The growth of oxide layers is promoted by OP-TMF conditions as compared to isothermal LCF conditions. Under OP-TMF conditions, oxide layers grow faster, in the absence of obvious spalling processes. Moreover, OP-TMF loading promotes brittle cracking of the oxide layer under tensile load at lower temperatures contributing to the lower lifetimes when compared to isothermal LCF loading.

(5) High temperature oxidation is an important part of OP-TMF crack nucleation and growth. A reaction layer forms on the crack flanks of OP-TMF cracks, consisting of an outer oxide layer and an inner zone depleted of oxide forming elements. Assuming early crack nucleation and cycle-by-cycle crack growth, one can derive parabolic growth laws for oxidation and for the growth of a depleted zone below the oxide layer. The slower growth of the oxide layer controls the rate of the two combined reactions. Once the oxide has reached a thickness of 2 µm, compression stress-assisted spalling suppresses further oxide layer growth. The fact that the depleted zone keeps growing shows that oxidation goes on. When the oxide no longer grows, the depleted zone layer growth is no longer constrained by the growing oxide layer and proceeds at a higher rate.

Acknowledgment

All authors acknowledge funding through project A1 and A2 of the collaborative research center SFB/TR 103 funded by the Deutsche Forschungsgemeinschaft (DFG).

Data Availability

The raw/processed data required to reproduce these findings cannot be shared at this time as the data also forms part of an ongoing study.

References

[1] M. McLean, Directionally solidified materials for high temperature service, The Metals Society, London, 1983. ISBN: 978-09043-5752-3

[2] J. Lacaze, A. Hazotte, Directionally solidified materials - Nickel-base superalloys for gas-turbines, Textures Microstruct., 13 (1990) 1-14. https://doi.org/10.1155/Tsm.13.1

[3] M. Durand-Charre: The microstructure of superalloys, CRC Press, 1998. ISBN: 978-9-05699-097-8

[4] M.J. Donachie, S.J. Donachie, Superalloys: A technical guide, second ed., ASM International, 2002. ISBN: 978-0-87170-749-9

[5] R.C. Reed, The superalloys: Fundamentals and applications, Cambridge University Press, 2006. https://doi.org/10.1017/CBO9780511541285

[6] T.M. Pollock, S. Tin, Nickel-based superalloys for advanced turbine engines: Chemistry, microstructure, and properties, J. Propul. Power, 22 (2006) 361-374. https://doi.org/10.2514/1.18239

[7] G. Cailletaud, J. Cormier, G. Eggeler, V. Maurel, L. Nazé (Editors): Nickel base single crystals across length scales, Elsevier, Amsterdam, 2022. ISBN: 978-0-12819-357-0

[8] W. Boas, R.W.K. Honeycombe, Thermal fatigue of metals, Nature, 154 (1944) 338. https://doi.org/10.1038/154338a0

[9] D.A. Spera, Thermal fatigue of materials and components, ASTM International, West Conshohocken, 1976. https://doi.org/10.1520/STP612-EB

[10] R.P. Skelton, High temperature fatigue, Elsevier Applied Sciences, Amsterdam, 1987. ISBN: 978-9-40108-046-0

[11] A.J. Weronski, T. Hejwowksi, Thermal fatigue of metals, Marcel Dekker Inc., New York, 1991. ISBN: 978-1-48227-683-1

[12] S. Suresh, Fatigue of materials, Cambridge University Press, Cambridge, 1991. https://doi.org/10.1017/CBO9780511806575

[13] H. Sehitoglu, H.J. Maier, Thermo-mechanical fatigue behavior of materials, STP 1371, ASTM International, West Conshohoken, 2000. https://doi.org/10.1520/STP1428-EB

[14] A. Pineau, S.D. Antolovich, High temperature fatigue of nickel-base superalloys – A review with special emphasis on deformation modes and oxidation, Eng. Fail. Anal., 16 (2009) 2668-2697. https://doi.org/10.1016/j.engfailanal.2009.01.010

[15] A. Pineau, S.D. Antolovich, High temperature fatigue: behaviour of three typical classes of structural materials, Mater. at High Temp., 32 (2015) 298-317. https://doi.org/10.1179/0960340914Z.00000000072

[16] J. Reuchet, L. Rémy, Fatigue oxidation interaction in a superalloy—Application to life prediction in high temperature low cycle fatigue, Metall. Trans. A, 14 (1983) 141-149. https://doi.org/10.1007/BF02643747

[17] J. Reuchet, L. Rémy, High temperature low cycle fatigue of MAR-M 509 superalloy I: The influence of temperature on the low cycle fatigue behaviour from 20 to 1100°C, Mater. Sci. Eng., 58 (1983) 19-32. https://doi.org/10.1016/0025-5416(83)90134-9

[18] P.K. Wright, Oxidation-fatigue interactions in a single-crystal cuperalloy, ASTM STP 942 (1988) 558-575. https://doi.org/10.1520/STP24506S

[19] N. Marchand, R. Pelloux, B. Ilschner, A fracture mechanics criterion for thermal-mechanical fatigue crack growth of gas turbine materials, Eng. Fract. Mech., 31 (1988) 535-551. https://doi.org/10.1016/0013-7944(88)90095-1

[20] A. Nitta, K. Kuwabara, Thermal-Mechanical Fatigue Failure and Life Prediction, in: R. Ohtani, M. Ohnami, T. Inoue (Eds.), High temperature creep-fatigue - Current japanese materials research - Vol. 3, Elsevier Applied Science (1988) 203-222.

[21] E. Fleury, L. Rémy, Low cycle fatigue damage in nickel-base superalloy single crystals at elevated temperature, Mater. Sci. Eng. A, 167 (1993) 23-30. https://doi.org/10.1016/0921-5093(93)90332-9

[22] E. Fleury, L. Rémy, Behavior of nickel-base superalloy single crystals under thermal-mechanical fatigue, Met. Mater. Trans. A, 25 (1994) 99-109. https://doi.org/10.1007/BF02646679

[23] S.A. Kraft, H. Mughrabi, Thermo-mechanical fatigue of the monocrystalline nickel-based superalloy CMSX-6, ASTM STP 1263 (1996) 27-40. https://doi.org/10.1520/STP16444S

[24] H. Mughrabi, S. Kraft, M. Ott, Specific aspects of isothermal and anisothermal fatigue of the monocrystalline nickel-base superalloy CMSX-6, Superalloys 1996 (1996) 335-344. http://dx.doi.org/10.7449/1996/Superalloys_1996_335_344

[25] F.F. Meyer-Olbersleben, C.C. Engler-Pinto, Jr., F. Rezai-Aria, On thermal fatigue of nickel-based superalloys, ASTM STP 1263 (1996) 41-55. https://doi.org/10.1520/STP16445S

[26] R.P. Skelton, Crack initiation and growth during thermal transients, in: J. Ginsztler, R.P. Skelton (Eds.), Component reliability under creep-fatigue conditions. International Centre for Mechanical Sciences, Springer, Vienna, 1998, 17-86. https://doi.org/10.1007/978-3-7091-2516-8_2

[27] M.M. Shenoy, A.P. Gordon, D.L. McDowell, R.W. Neu, Thermomechanical fatigue behavior of a directionally solidified Ni-base superalloy., ASME J. Eng. Mater. Technol., 127 (2005) 325–336. https://doi.org/10.1115/1.1924560

[28] M. Okazaki, M. Sakaguchi, Thermo-mechanical fatigue failure of a single crystal Ni-based superalloy, Int. J. Fatigue, 30 (2008) 318-323. https://doi.org/10.1016/j.ijfatigue.2007.01.044

[29] J.J. Moverare, S. Johansson, R.C. Reed, Deformation and damage mechanisms during thermal–mechanical fatigue of a single-crystal superalloy, Acta Mater., 57 (2009) 2266-2276. https://doi.org/10.1016/j.actamat.2009.01.027

[30] H.U. Hong, J. G. Kang, B. G. Choi, I.S. Kim, Y.S. Yoo, C.Y. Jo, A comparative study on thermomechanical and low cycle fatigue failures of a single crystal nickel-based superalloy, Int. J. Fatigue, 33 (2011) 1592-1599. https://doi.org/10.1016/j.ijfatigue.2011.07.009

[31] S. Guth, Schädigung und Lebensdauer von Nickelbasislegierung unter thermisch-mechanischer Ermüdungsbeanspruchung bei verschiedenen Phasenlagen, Dr.-Ing. Thesis, Karlsruhe Institute of Technology (KIT), Karlsruhe, 2015. https://doi.org/10.5445/KSP/1000049869

[32] S. Guth, S. Doll, K.H. Lang, Influence of phase angle on lifetime, cyclic deformation and damage behavior of Mar-M247 LC under thermo-mechanical fatigue, Mat. Sci. Eng. A, 642 (2015) 42-48. https://doi.org/10.1016/j.msea.2015.06.055

[33] S. Guth, R. Petráš, V. Škorík, T. Kruml, J. Man, K.-H. Lang, J. Polák, Influence of dwell times on the thermomechanical fatigue behavior of a directionally solidified Ni-base superalloy, Int. J. Fatigue, 80 (2015) 426-433. https://doi.org/10.1016/j.ijfatigue.2015.07.005

[34] A. Thakur, S. Gangopadhyay, State-of-the-art in surface integrity in machining of nickel-based super alloys, Int. J. Mach. Tools Manuf., 100 (2016) 25-54. https://doi.org/10.1016/j.ijmachtools.2015.10.001

[35] D. Wu, D. Zhang, C. Yao, Effect of turning and surface polishing treatments on surface integrity and fatigue performance of nickel-based alloy GH4169, Metals, 8 (2018) article no. 549. https://doi.org/10.3390/met8070549

[36] C. Meid, M. Eggeler, P. Watermeyer, A. Kostka, T. Hammerschmidt, R. Drautz, G. Eggeler, M. Bartsch, Stress-induced formation of TCP phases during high temperature low cycle fatigue loading of the single-crystal Ni-base superalloy ERBO/1, Acta Mater., 168 (2019) 343-352. https://doi.org/10.1016/j.actamat.2019.02.022

[37] Z.R. Wu, S.Q. Wang, X. Yang, L. Pan, Y.D. Song, Fatigue life prediction for Ni-based superalloy GH4169 considering machined surface roughness and residual stress effects, J. Theor. Appl. Mech., 59 (2021) 215-226. http://dx.doi.org/10.15632/jtam-pl/132951

[38] I. Sulak, K. Obrtlík, T. Babinský, S. Guth, The low cycle fatigue behaviour of MAR-M247 superalloy under different strain rates and cycle shapes at 750°C, Int. J. Fatigue, 164 (2022) article no. 107133. https://doi.org/10.1016/j.ijfatigue.2022.107133

[39] C. Luo, H. Yuang, Aniostropic thermomechanical fatigue of a nickel-base single-crystal superalloy. Part I: Effects of crystal orientation and damage mechanisms, Int. J. Fatigue, 168 (2023) article no. 107438. https://doi.org/10.1016/j.ijfatigue.2022.107438

[40] I. Šulák, K. Obrtlík, The effect of dwell on thermomechanical fatigue behaviour of Ni-base superalloy Inconel 713LC, Int. J. Fatigue, 166 (2023) article no. 107238. https://doi.org/10.1016/j.ijfatigue.2022.107238

[41] V.H. Dao, H.S. Yun, J.S. Koo, P. Jaeyeong, S.H. Nahm, Experimental investigation of thermomechanical fatigue behavior in directionally solidified Ni-based superalloy under in-phase and out-of-phase conditions, J. Alloys Compd., 990 (2024) article no. 174430. https://doi.org/10.1016/j.jallcom.2024.174430

[42] H. Zhou, M. Osawa, H. Harada, T. Yokokawa, Y. Koizumi, T. Kobayashi, M. Waki, Y. Ro, I. Okada, A Comparative Study of Thermo-Mechanical Fatigue of Two Ni-based Single Crystal Superalloys, Superalloys 2004 (2004) 225-232.

[43] D. Arrell, M. Hasselqvist, C. Sommer, J. Moverare, On TMF damage, degradation effects, and the associated T^{min} influence on TMF test results in γ/γ' alloys, Superalloys 2004 (2004) 291-294.

[44] M. Kolbe, The high temperature decrease of the critical resolved shear stress in nickel-base superalloys, Mat. Sci. Eng. A, 319 (2001) 383-387. https://doi.org/10.1016/S0921-5093(01)00944-3

[45] X. Wu, P. Wollgramm, C. Somsen, A. Dlouhy, A. Kostka, G. Eggeler, Double minimum creep of single crystal Ni-base superalloys, Acta Mater., 112 (2016) 242-260. https://doi.org/10.1016/j.actamat.2016.04.012

[46] X. Wu, A. Dlouhy, Y.M. Eggeler, E. Spiecker, A. Kostka, C. Somsen, G. Eggeler, On the nucleation of planar faults during low temperature and high stress creep of single crystal Ni-base superalloys, Acta. Mater., 144 (2018) 642-655. https://doi.org/10.1016/j.actamat.2017.09.063

[47] A.B. Parsa, P. Wollgramm, H. Buck, C. Somsen, A. Kostka, I. Povstugar, P.P. Choi, D. Raabe, A. Dlouhy, J. Mueller, E. Spiecker, K. Demtroeder, J. Schreuer, K. Neuking, G. Eggeler, Advanced scale bridging microstructure analysis of single crystal Ni-base superalloys, Adv. Eng. Mat., 17 (2014) 216-230. https://doi.org/10.1002/adem.201400136

[48] Imagic Bildverarbeitung AG. (2015). Imagic Image Managing System (IMS) (V23H2) [Software]. https://www.imagic.ch/de/imagic-ims

[49] P. Thome, S. Medghalchi, J. Frenzel, J. Schreuer, G. Eggeler, Ni-base superalloy single crystal (SX) mosaicity characterized by the rotation vector base line electron back scatter diffraction (RVB-EBSD) method, Ultramicroscopy, 206 (2019) article no. 112817. https://doi.org/10.1016/j.ultramic.2019.112817

[50] L. Cao, P. Thome, L.A. Jacome, C. Somsen, G. Cailletaud, G. Eggeler, On the influence of crystallography on creep of circular notched single crystal superalloy specimens, Mater. Sci. Eng. A, 782 (2020) article no. 139255. https://doi.org/10.1016/j.msea.2020.139255

[51] S. Gamanov, A. Dlouhy, D. Burger, G. Eggeler, P. Thome, Evolution of local misorientations in the γ/γ'-microstructure of single crystal superalloys during creep studied with the

rotation vector baseline (RVB) EBSD method, Microsc. Res. Tech., (2023) 1-18. https://doi.org/10.1002/jemt.24453

[52] L. Heep, D. Bürger, C. Bonnekoh, P. Wollgramm, A. Dlouhy, G. Eggeler, The effect of deviations from precise [001] tensile direction on creep of Ni-base single crystal superalloys, Scripta Mater., 207 (2022) article no. 114274. https://doi.org/10.1016/j.scriptamat.2021.114274

[53] P. Wollgramm, H. Buck, K. Neuking, A.B. Parsa, S. Schuwalow, J. Rogal, R. Drautz, G. Eggeler, On the role of Re in the stress and temperature dependence of creep of Ni-base single Crystal superalloys, Mat. Sci. Eng. A, 628 (2015) 382-395. https://doi.org/ 10.1016/j.msea.2015.01.010

[54] P. Wollgramm, D. Bürger, A.B. Parsa, K. Neuking, G. Eggeler, The effect of stress, temperature and loading direction on the creep behavior of Ni-base single crystal superalloy miniature specimens, Mater. at High Temp., 33 (2016) 346-360. https://doi.org/10.1080/09603409.2016.1186414

[55] P. Hallensleben, H. Schaar, P. Thome, N. Jöns, A. Jafarizadeh, I. Steinbach, G. Eggeler, J. Frenzel, On the evolution of cast microstructures during processing of single crystal Ni-base superalloys using a Bridgman seed technique, Mater. Des., 128 (2017) 98-111. https://doi.org/10.1016/j.matdes.2017.05.001

[56] D. Whitehouse, Surfaces and their measurement, Butterworth-Heinemann, Boston, 2012. ISBN: 978-0-08097-201-5

[57] P. Hähner, E. Affeldt, T. Beck, H. Klingelhöffer, M. Loveday, C. Rinaldi, Validated code-of-practice for strain-controlled thermo-mechanical fatigue testing. EUR 22281 EN – DG JRCC-Insitute for Energy, Office for Offical Publications of the European Communities, Luxemburg, 2006. ISBN 92-79-02216-4

[58] A. Sato, Y.L. Chiu, R.C. Reed, Oxidation of nickel-based single-crystal superalloys for industrial gas turbine applications, Acta Mater., 59 (2011) 225-240. https://doi.org/10.1016/j.actamat.2010.09.027

[59] J. Pistor, S.P. Hagen, S. Virtanen, C. Körner, Influence of the microstructural homogeneity on the high-temperature oxidation behavior of a single crystalline Ni-base superalloy, Scripta Mater., 207 (2022) article no. 114301. https://doi.org/10.1016/j.scriptamat.2021.114301

[60] K. Demtröder, G. Eggeler, J. Schreuer, Influence of microstructure on macroscopic elastic properties and thermal expansion of nickel-base superalloys ERBO/1 and LEK94, Mat.-wiss. u. Werkstofftech., 46 (2015) 563-576. https://doi.org/10.1002/mawe.201500406

[61] S. Baik, R, Raj, Mechanisms of creep-fatigue interaction, Met. Trans. A, 13 (1982) 1215-1221. https://doi.org/10.1007/BF02645504

[62] J.K.S. Jadon , R. Singh, J.K. Mahato, Creep-fatigue interaction behavior of high temperature alloys: A review, Materials Today Proceedings, 62 (2022) 5351-5357. https://doi.org/10.1016/j.matpr.2022.03.487

[63] J.C. Earthman, G. Eggeler, B. Ilschner, Deformation and damage processes in a 12%Cr-Mo-V steel under high temperature low cycle fatigue conditions in air and vacuum, Mat. Sci. Eng. A, 110 (1989) 103-114. https://10.1016/0921-5093(89)90161-5

[64] C. Wagner, Beitrag zur Theorie des Anlaufvorgangs, Z. phys. Chem., 21B (1933) 25-41. https://doi.org/10.1515/zpch-1933-2105

[65] S. Mrowec, An introduction to the theory of metal oxidation, National Bureau of Standards and National Science Foundation, Washington D.C., 1982.

[66] P. Kofstad, High temperature corrosion, Elsevier Applied Science, London and New York, 1988. ISBN 1-85166-154-9

[67] M.G: Hebsur, R.V: Miner, High temperature isothermal and cyclic oxidation behavior of a single crystal Ni-base superalloy, Mater. Ener. Syst., 8 (1987) 363-370. https://doi.org/10.1007/BF02833484

[68] J.L. Smialek, Oxide morphology and spalling model for NiAl, Metall. Trans. A, 9 (1978) 309-320. https://doi.org/10.1007/bf02646380

[69] D. Poquillon, D. Monceau, Application of a simple statistical spalling model for the analysis of high-temperature, cyclic-oxidation kinetics data, Oxid. Met., 59 (2003) 409-431. https://doi.org/10.1023/a:1023004430423

[70] O.M. Horst, D. Schmitz, J. Schreuer, P. Git, H. Wang, C. Körner, G. Eggeler, Thermoelastic properties and γ'-solvus temperatures of single-crystal Ni-base superalloys, J. Mater. Sci., 56 (2021) 7637-7658. https://doi.org/10.1007/s10853-020-05628-w

Declaration of interests

☒ The authors declare that they have no known competing financial interests or personal relationships that could have appeared to influence the work reported in this paper.

☐The authors declare the following financial interests/personal relationships which may be considered as potential competing interests: